Desalination and Water Treatment
www.deswater.com

doi: 10.5004/dwt.2020.25958

197 (2020) 14–29
September

Predicting the scaling rate of calcium carbonate in wet-gas pipes via a CFD method

Changjun Li, Bo Wang*, Wenlong Jia, Guiliang Li

Petroleum Engineering School, Southwest Petroleum University, 8 Xindu Road, Xindu District, Chengdu 610500, China, emails: wofeiziwozai@hotmail.com (B. Wang), 942720019@qq.com (C.J. Li), jiawenlong08@126.com (W.L. Jia), liguiliang@aliyun.com (G.L. Li)

Received 12 September 2019; Accepted 9 April 2020

ABSTRACT

The scaling of the wet-gas pipes is getting worse along with the increasing volume of produced water, and can increase energy consumption, and even cause blockage accidents. Hence, the accurate prediction of the scaling rate is crucial for the effective and safe operation of pipelines. In this paper, a computation fluid dynamic (CFD) method based on the combination of chemical reaction model, discrete phase model (DPM), erosion model (EM) and fluid-structure interaction model can estimate the scale formation and deposition process and rate in straight pipelines and elbows. The two key parameters, the exponential factor and the temperature index used to calculate the scale formation rate, are fitted from scale experimental data collected from a field wet-gas transmission pipe. Based on the sedimentary probability obtained by DPM and EM, the scaling rate calculation model (SRCM) established. The experiment items study for wet-gas pipelines demonstrates CFD-SRCM; the relative deviation between the actual scale rate and the calculated value is in the range of 2.7% to 18.9%. And then, two industrial cases forecast the scaling rates. CFD-SRCM is a highly promising new method for predictive monitoring of scaling.

Keywords: Wet-gas pipes; Scaling rate; Numerical Simulation; Chemical reaction rate; CFD-SRCM

1. Introduction

In the development of gas reservoirs, connate fluids often intrude into the reservoir and finally flow to the surface together with the natural gas [1], forming the "produced water" [2]. Produced water usually contains high concentrations of many kinds of cations, including the calcium (Ca^{2+}), magnesium (Mg^{2+}), barium (Ba^{2+}), strontium (Sr^{2+}), and anions including hydrogen carbonate (HCO_3^-), sulfate (SO_4^{2-}) et al. [3,4]. These ions are natural to form scale in pipelines, resulting in the reduction of internal diameters of pipes and elbows [5,6]. So, it is essential to understand the scaling mechanism and rate for the reduction of energy consumption and economic cost and the improvement of the pipeline life.

Based on the experimental data, many theoretical and numerical simulation methods have been proposed to research the scaling problems in the wet-gas pipelines. Since the 1950s, much academic research on scaling during the exploitation process of the gas field has studied. Kern and Seaton [7,8] firstly proposed a typical mathematical model of scaling, which divided into scaling deposition and scaling denudation. Hasson et al. [9,10] established an ion diffusion model to depict the precipitation process of calcium carbonate ($CaCO_3$) crystals, which considers the effects of ion concentration, temperature, pressure, and other factors on the scaling rate. It showed that Ca^{2+} and HCO_3^- firstly moves to the inner pipe wall, and then forms $CaCO_3$ on the wall surface through a chemical reaction, and finally crystallized and scaled on the wall surface.

* Corresponding author.

Amiri et al. [11] presented the predicting of $CaCO_3$ precipitation in formation water, injection water, and mixing of injection water with formation water at different pressures and used OLI ScaleChem software to determine the amount of $CaCO_3$ scale. Kamari et al. [12] presented the least square support vector machine optimized with a simulated annealing optimization strategy, statistical and graphical error analyses to estimate the potential deposition from an equilibrated $CaCO_3$ aqueous phase. Two-hundred series of literature-reported data of correction factor (*K*) [13] as a function of temperature and total ionic strength were used to test the Kamari model. The model developed provides estimations which are in good agreement with literature data.

The scaling rate rules of produced water have reported [14–16]. Vetter et al. [17] predict the co-precipitation of $CaCO_3$, barium sulfate ($BaSO_4$), strontium sulfate ($SrSO_4$) and calcium sulfate ($CaSO_4$) at various locations, temperatures, and pressures in waterflood operations. Kan and Tomson [18] verify the accuracy of the Pitzer ion-interaction model-based scale-prediction algorithms. However, in most cases, the scaling rate rules of produced water are from the perspective of thermodynamics, without considering the hydrodynamic factors.

In particular, using the combination of the theory model, rate rules, and computation fluid dynamic (CFD) method represents a tendency to calculate the scaling conditions in various equipment, including the heater exchanger. This method solves the governor equations of fluids and particles in a coupled approach, which provides an effective way to analyze the effects of many factors on the scaling rate qualitatively. Brahim et al. [19] used FLUENT software to conduct CFD simulation, to calculate scale thickness and scale density, and to monitor the thermal flux distribution of solid surface in real-time, to predict scale thermal resistance and scale temperature distribution. Johnsen et al. [20] studied the wall deposition and boundary layer diffusion of multicomponent mixtures under turbulent. Xiao et al. [21] developed a three-dimensional CFD model, which used in the induction stage of dirt in microscale channels. Kuruneru et al. [22] presented a coupled finite volume model – discrete element method, which studies oscillating multiphase foulant-laden air (solid–gas) flow and particulate scaling in a porous heat exchanger channel which is consist of an array of circular cylinders. Souza et al. [23] presented a model that is composed of mass, energy, and mechanical energy balances, also contemplating the influence of the scaling rate in the heat exchangers. The simulation can determine the flow rates and temperatures along with the network for each time instant during the investigated period. The above results are the scaling of the heat exchanger pipe section; the amount and thickness of scale deduced from the thermal resistance and heat transfer coefficient. However, the temperature of wet-gas pipelines changes little, and the scaling amount and scaling rate cannot determine by temperature field analysis.

Given the above, it is difficult to predict the scaling rate in wet-gas pipes accurately because of the chemical reaction of scaling ions and hydrodynamic factors. In this paper, CFD-SRCM (SRCM – scaling rate calculation model) can predict the scaling rate of calcium carbonate and reveal the rules of scaling under the three-dimensional flow condition in wet-gas pipelines, including the straight pipe and the horizontal elbows with different bending radius. The experiment items study for wet-gas pipelines demonstrates CFD-SRCM.

2. Experiment and mechanism

2.1. Water sampling and mass of scaling

The three groups of produced water samples are collected from a gas field in southwest China, which suffers from serious scaling problems [24], shown in Fig. 1. The multi-function ion chromatography is used for qualitative and quantitative analysis of produced water samples and follows the method SY/T 5523-2016 "Method for analysis of oilfield water" (equivalent to API RP 45) [25,26].

The indoor scaling experiments use the collected water samples to research the mass of scaling in different temperatures based on the actual temperature range of the pipeline [27,28]. The collected water samples placed in the same environment as the collection point to observe phenomena. After some time, the produced water from the gas field filtered through a filter membrane. The scale formation amounts in the water samples calculated by the filtration volume of the water sample and the mass increase of the filter paper [29]. The results can provide a basis for setting parameters of the chemical model afterward.

2.2. Scale composition analysis

One scale sample is collected from the inner pipe wall in station A pipeline, shown in Fig. 1a. The scanning electron microscopy is applied to analyze the microstructure of scale [30,31]. The composition of the scale sample interpreted by the high-temperature weightless method and the energy-dispersive X-ray spectrometer (EDS) [26].

2.3. Scale deposition mechanism

The scale deposition mechanism of $CaCO_3$ scale formation is investigated. Flow parameters changing of anions and cations combined into scale particles in the pipeline [32]. The quantitative relation of HCO_3^-, CO_3^{2-} anions, CO_2, and Ca^{2+} cations determines the movement direction of the reaction, and the number of these anions and cations are affected by the external environment.

$$Ca^{2+} + CO_3^{2-} \rightarrow CaCO_3 \downarrow \tag{1}$$

$$Ca^{2+}_{(aq)} + 2HCO^-_{3(aq)} \rightleftharpoons CaCO_{3(s)} + CO_{2(aq)} + H_2O_{(l)} \tag{2}$$

The particles in the water are affected by various forces, which are gravity, buoyancy, inertial force, resistance, virtual mass force, Magnus lift force, Basset force, and Saffman lift force, and the flow trajectory will change correspondingly. By analyzing the force condition, the motion trajectory of the scale particles in the pipeline can obtain [33]. The scaling tendency of $CaCO_3$ in the produced water increases with the increase of scale ion concentration, temperature, pH value, and dissolved salt concentration, also with the decrease of CO_2 partial pressure [22]. And it is affected by

(a) (b)

Fig. 1. Scaling phenomenons of station A (a) pipeline and (b) valve in the gas field.

hydrodynamics factors such as flow state, flow environment, velocity, and its distribution [34]. Among them, four elements of more significant influence are scale ion concentration, temperature, salinity, and hydrodynamics [35].

The scale deposition mechanism of the $CaCO_3$ scale in the wet-gas pipe identified. Primarily, $CaCO_3$ particles formed by chemical reaction of scaling anions and cations in water. Furthermore, the crystals formed on the rough inner walls of the pipes and equipment and gradually separate. Eventually, the $CaCO_3$ scale is formed along with the scouring effect of the fluid [36,37], shown in Fig. 2.

Similar to $CaCO_3$, the chemical reaction of $CaSO_4$ and $BaSO_4$ shown in Eqs. (3) and (4).

$$Ca^{2+} + SO_4^{2-} \rightarrow CaSO_4 \downarrow \tag{3}$$

$$Ba^{2+} + SO_4^{2-} \rightarrow BaSO_4 \downarrow \tag{4}$$

3. Model framework

The hybrid model proposed in this paper combines CFD and SRCM, namely CFD-SRCM. The discrete phase model (DPM) model is established based on scaling mechanism theory and Kern–Seaton model theory, and considered the force of the scale particles and the combination of erosion and deposition, using chemical reaction model (CRM), DPM, erosion model (EM) and fluid-structure interaction model (FSIM) [38]. Based on the sedimentary probability obtained by DPM and EM, SRCM established. The framework of CFD-SRCM presented in Fig. 3. The rule of migration and settlement of scale particles in the pipeline studied from the perspective of hydrodynamics, and the scaling rate is analyzed.

3.1. CFD model

In the CFD model, it assumed that all for field produced water in the pipeline and gas-free, ignore the two-phase flow's influence on the scaling rate, due to the scaling ions exist in the produced water. The Eulerian–Lagrangian approach is employed to capture the flow properties of water flow and particle tracking of $CaCO_3$ particles [39]. Due to the short local component, the produced waters treated as incompressible fluids, and the whole flow field calculated by the Eulerian approach. The liquid in the pipeline must satisfy the following three rules: the mass, momentum, and energy balances [20,23,40]. The three control equations of continuous phase fluid expressed as:

$$\frac{\partial \rho_L}{\partial t} + \frac{\partial(\rho_L u_i)}{\partial x_i} = S_M \tag{5}$$

$$\frac{\partial(\rho_L u_i)}{\partial t} + \frac{\partial(\rho_L u_i u_j)}{\partial x_j} = -\frac{\partial p}{\partial x_i} + \frac{\partial\left(\mu \frac{\partial u_i}{\partial x_j} - \rho_L \overline{u_{ip} u_{jp}}\right)}{\partial x_j} + S_{MO} \tag{6}$$

$$\frac{\partial(\rho_L T)}{\partial t} + \frac{\partial(\rho_L u_i T)}{\partial x_i} = \frac{\partial\left(\frac{k}{C_P}\frac{\partial T}{\partial x_i}\right)}{\partial x_i} + S_E \tag{7}$$

where ρ_L is the density of the liquid, S_M is the source term of the mass equation, S_{MO} is the source term of the momentum equation, u_i and u_j are the average velocity components of the liquid, u_{ip} and u_{jp} are the pulsation velocity components of the liquid, and S_E is the source term of the energy equation.

The turbulence at the elbows includes the flow of rapids and the deposit of the scales on the wall. Therefore, the re-normalization group (RNG) k-ε model chosen as the turbulence model. The transport equations associated with turbulent kinetic energy and energy dissipation rate in turbulent expressed as [39,41]:

$$\frac{\partial(\rho_L k)}{\partial t} + \frac{\partial(\rho_L k u_i)}{\partial x_i} = \frac{\partial}{\partial x_j}\left[\gamma_k u_{\text{eff}} \frac{\partial k}{\partial x_j}\right] + G_K - \rho_L \varepsilon \tag{8}$$

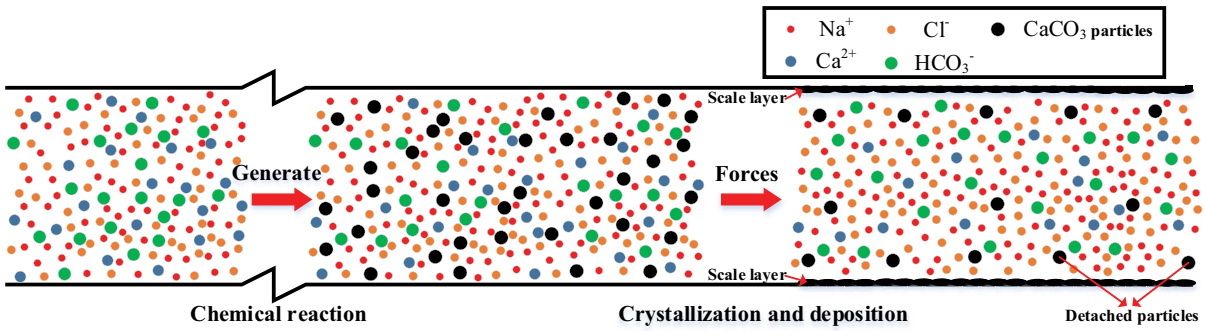

Fig. 2. Schematic diagram of the scaling process of the $CaCO_3$ scale.

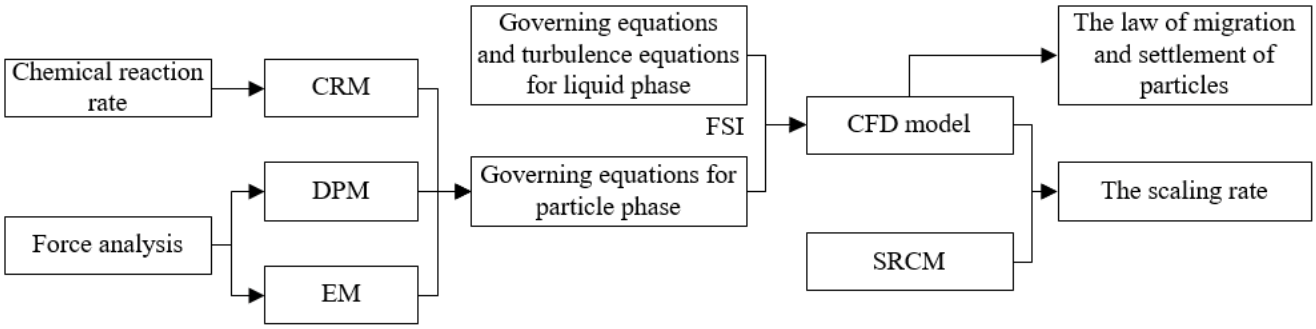

Fig. 3. The framework of CFD-SRCM.

$$\frac{\partial(\rho_L\varepsilon)}{\partial t}+\frac{\partial(\rho_L\varepsilon u_i)}{\partial x_i}=\frac{\partial}{\partial x_j}\left[\gamma_\varepsilon u_{\text{eff}}\frac{\partial\varepsilon}{\partial x_j}\right]+\frac{C_{1\varepsilon}\varepsilon}{k}G_k-C_{2\varepsilon}O_L\frac{\varepsilon^2}{k} \tag{9}$$

where G_k is the turbulent kinetic energy caused by the mean velocity gradient. γ_k and γ_ε are Prandtl number. $C_{1\varepsilon}$ and $C_{2\varepsilon}$ are the empirical constants taken as 1.44 and 1.92.

The governing equations for the particle phase use the unsteady Reynolds-Averaged Navier–Stokes (URANS) equations to calculate the flow field and use the Lagrangian approach to describe the scale particles [39]. In the Cartesian coordinate system, the force balance equation of the scale particles is the inertia of the scale particles is equal to the forces acting on the scale particles:

$$\frac{du_p}{dt}=\frac{3\mu C_D\,\text{Re}}{4\rho_p d_p^2}\left(u-u_p\right)+\frac{g\left(\rho_p-\rho_L\right)}{\rho_p}+F \tag{10}$$

where C_D is the drag coefficient, Re is the Reynolds number, ϱ_p is the density of scale particles, d_p is the diameter of scale particles. The power of the scale particles in the field (F) mainly includes visual mass force (F_{vm}), Magnus force (F_M), Basset force (F_B), and Saffman lift force (F_S).

The velocity is adapted to calculate the trajectory of the scale particles through Eq. (11). And the diffusion of the scale particles derives through the instantaneous velocity generated by velocity pulsation. Using the trapezoid difference method to solve Eqs. (10) and (11) at the same time, and then the velocity and position of the scale particles can be obtained.

$$\frac{dx}{dt}=u_p \tag{11}$$

The scaling rate is composed of deposition rate (v_d) and removal rate (v_r) under the scouring effect of the fluid. The removal rate is relative to the thickness of the scale and shear force of the fluid on the level.

$$v_d=\sum_{n=1}^{N}\frac{M_p}{A_{\text{face}}} \tag{12}$$

$$v_r=\sum_{n=1}^{N}\frac{M_p f(\alpha)u_p^{b(u_p)}}{A_{\text{face}}} \tag{13}$$

in which

$$f(\alpha)=\begin{cases}-38.4\alpha^2+22.7\alpha & (\alpha<0.267)\\ 3.147\cos^2\alpha\sin\alpha+0.3609\sin^2\alpha+2.532 & (\alpha\geq 0.267)\end{cases} \tag{14}$$

where N is the number of scale particles, M_p is the mass flow of particles, A_{face} is a projected area of scale particles on the wall, α is the impact angle of particles on the wall surface, $f(\alpha)$ is a function of impact angle, and $b(u_p)$ is a function of the velocity taken as 1.73 [42].

Therefore, the actual scaling rate expressed as:

$$\frac{dm}{dt} = v_d - v_r \tag{15}$$

Meanwhile, the motion trajectory of solid scale particles in the pipeline is obtained, which provides a theoretical basis for analyzing the migration and settlement rule of scale particles in various local components.

For scaling of the wet-gas pipelines, scaling ions, and water slowly into the reaction zone, in the reaction zone occurs rapidly reversible chemical reaction and influential hydrodynamic factors in controlling the response. The scaling process involves the mixing, transport, and reaction of scale ions. The forward reaction rate constant (C_f) calculates by Arrhenius formula:

$$C_f = AT^{\beta}e^{-E/RT} \tag{16}$$

where E is the reaction activation energy, 46,600 J mol^{-1} and R is the gas constant, 8.314 J mol^{-1} K^{-1}.

In Eq. (16), there are two critical parameters, including the exponential factor (A) and the temperature index (β). They are directly related to the generating amount of $CaCO_3$ scale particles, particle migration, and deposition behavior in the pipeline. Certain chemical reactions have a specific reaction rate constant (C).

For the reaction, the concentration and pressure of the reactants will not change the C value, but the temperature will affect the C value. The C of scale particles is closely related to pressure, temperature, and scale ion concentration. Therefore, the scale of the chemical reaction rate constant is changing in the pipe, but the index factor fixes. The rate of the chemical reaction (r) (Eq. (2)) can calculate using Eq. (17) [15].

$$r = Cc_{Ca^{2+}}c^2_{HCO_3^-} \tag{17}$$

The generating amount of $CaCO_3$ scale can calculate using the r.

$$m = r \cdot \Delta t \cdot M_{CaCO_3} \tag{18}$$

where Δt is the scaling time. M_{CaCO_3} is the molecular mass of $CaCO_3$.

3.2. Numerical approach

The above CFD model is solved by the generic commercial code ANSYS 16.0, which includes the FLUENT module used to calculate flow field. The FSI simulation is conducted on the FLUENT, which is a fluid-structure interaction computing platform based on a staggered FSI approach. URANS, DPM, EM, and CRM are contained in FLUENT. Comprehensive comparison choose the Eddy-dissipation concept module in the finite rate model, which considers the detailed chemical reaction mechanism in the turbulent flow and is more suitable for the reversible chemical reaction.

The chemical reactions occur continuously between the scaling anions and cations. The scale particles in the pipeline continuously are depositing and exchanging heat, mass, and momentum with the liquid phase. Therefore, the calculation of the liquid phase and the scale particles should be coupled. By alternately solving the control equation of the discrete phase and continuous phase, the purpose of both convergences achieved, which is the calculation solution of the both is not changed, and the two-way coupling calculation completed [36,37].

Due to the produced water in the process of the flow, it contains scaling ions react, generate scale particles gradually, but its total mass did not change. It's just that the total mass of the water is decreasing, the total mass of the solid particles is increasing, and the change is consistent.

The coupling between the discrete phase and the continuous phase mainly refers to the coupling of momentum in the pipeline. When the scale particles flow in the produced water, through the calculation of the momentum change of the scale particles, the momentum value between the scale particles and the produced water obtains. This value will use in the calculation of the following liquid phase equation, and the bidirectional coupling calculation realizes.

When the scale particles are in the process of produced water, the energy will transfer between the scale particles, the scale particles, and the produced water. By calculating the energy change of the scale particles, the energy of the water transfer to the scale particles obtains. It assumes that the internal heat resistance of the scale particles is zero; namely, their temperature is consistent everywhere.

The pressure-velocity coupling method selected as coupled, so the spatial discretization of pressure, momentum, and each component adapt the second-order upwind mode. The turbulence kinetic energy and the turbulence dissipation rate is selected as the first-order upwind mode to ensure the convergence of turbulence.

3.3. Scaling rate calculation model

In the case of $CaCO_3$ particles moving in local components, the deposition probability (ϕ_{dep}) is an important parameter to investigate the scaling rate and amount of scale. SRCM is established based on the probability and mass of $CaCO_3$ particles deposition calculated by the CFD model. The following equations express the computational process of SRCM.

$$\phi_{dep} = \frac{N_{trap}}{N_{trap} + N_{escape}} \times 100\% \tag{19}$$

where N_{trap} is the number of $CaCO_3$ particles captured by the wall of the pipeline. N_{escape} is the number of $CaCO_3$ particles escaping from the exit.

Initially, the actual deposition of $CaCO_3$ mass fraction expressed as:

$$m_f = m_p \times \phi_{dep} \tag{20}$$

where m_p is the resulting $CaCO_3$ mass fraction. And afterward, the daily scale amount of $CaCO_3$ can obtain by calculate the actual deposition of the $CaCO_3$ mass fraction through Eq. (21).

$$m_{\mathrm{ds}} = m_f \times \rho_L \times 3600 \times 10^6 \tag{21}$$

Because of the existing technology and measures to protect the pipeline, only the thickness of the scale can measure, and it is impossible to clean out the pipe scale and weigh it. Finally, the thickness of the corresponding pipe scale layer can obtain through Eq. (22).

$$l = \frac{m_{\mathrm{ds}} \times 24 \times t_{\mathrm{run}} \times 10^{-3}}{d_{\mathrm{in}} \times \pi \times \rho_p} \times 10 \tag{22}$$

where l is the thickness of the scale layer, t_{run} is the running day for the pipeline, d_{in} is the diameter of the pipe inlet surface.

3.4. Boundary conditions

The inlet and exit boundary conditions are velocity inlet conditions and outflow boundary conditions, respectively. The inlet velocity value is based on the actual operating range. Turbulence intensity and hydraulic diameter describe the turbulence of the boundary layer flow and its full development. The pipe wall boundary condition is the no-slip condition.

The initial condition of the DPM model is a surface jet source. The surface is the inlet interface. The particle type is $CaCO_3$ particle, and its density is 2,800 kg m^{-3}. To ensure that the number of particles entering the pipeline is the same in the unit time, the mass flow of $CaCO_3$ particles in each local component under different conditions set to 1×10^{-20}kg s^{-1}. The volume concentration of $CaCO_3$ particles in pipe and elbows calculated through Eq. (23), and all of them are less than 10%, which meets the requirements of the DPM model.

$$\eta = \frac{4m_{\mathrm{pv}}}{\pi \rho_{\mathrm{p}} d_{\mathrm{in}}^2 u_{\mathrm{in}}} \times 100\% \tag{23}$$

where η is $CaCO_3$ particle volume concentration, m_{pv} is $CaCO_3$ particle mass flow velocity, u_{in} is the inlet fluid velocity.

Since the model simulates the deposition of $CaCO_3$ particles on the pipe wall, the wall surface of the DPM model configures as trap conditions.

3.5. Simulation parameters and computational mesh

The pipeline in the station A determines as DN100, with the inner diameter of 95 mm and the outer diameter of 114 mm. The length of the straight pipe section is 2,500 mm. The physical model of the straight pipe is constructed based on model parameters, shown in Fig. 4a. The center of the inlet is the origin of coordinates. The positive direction of the X-axis is the direction of the flow. The other end of the pipe is the outlet, and its gravity direction is the negative direction of the Y-axis. For the single boundary of the straight pipe, the flow field can directly divide into the structural grid. The grid has the advantages of orderly arrangement, good quality, rapid generation, and simple structure. Boundary layer meshing uses the wall function method to ensure that y^+ is between 30 and 60. A total of 253,680 nodes generated in the flow field by comprehensively analyzing the accuracy of calculation results (Fig. 5) and the efficiency of computer simulation, shown in Fig. 4b.

The bending radii of the actual elbows are 210 and 315 mm. To make the results more accurate, so the bending radii of the horizontal elbows are 105, 210, 315, 420, and 525 mm. Meanwhile, a 350 mm straight pipe is added at the inlet and outlet of the elbow to ensure the accuracy of the flow field analysis results. When the number of nodes of the elbow with a bending radius of 105 mm is 113,760, the number of nodes will continue to increase, and the mass score of $CaCO_3$ will not change significantly. Therefore, 113,760 nodes generate for flow field division by independence, shown in Fig. 6. Similar to the elbow with the bending radius of 105 mm, grid divisions of the other elbows carried out. Besides, grid independence is verified and analyzed. Finally, the number of nodes in the other elbows is obtained. The number of nodes in the elbow with a bending radius of 210, 315, 420, and 525 mm is 119,412; 129,860; 151,632; and 164,283, respectively.

The produced water sample's quality serves as the initial species and concentration of anions and cations in the model. Due to the small length of the simulated pipeline, the temperature changes little, ignoring the change of the chemical reaction rate constant. Based on the analysis of scaling factors, selecting temperature, scaling ionic concentration, particle size, and flow velocity as the research factors [36]. According to the actual operation data and research results, and in the simulation process of the straight pipe section, a comparison project of scale ion concentration added, and the specific schemes for the simulation of straight pipe and horizontal elbow are shown in Tables 1 and 2.

4. Results and discussion

4.1. Experiment results

The produced water samples' quality is presented in Table 3. The pH values of the water samples are between 6.63 and 6.72, which is slightly acidic. Their mineralization degrees are higher. The water samples contain a high concentration of Ca^{2+}, Mg^{2+}, Ba^{2+}, Sr^{2+} cations, and HCO_3^- anions. Under specific temperature and pressure conditions, the chemical equilibrium equation of insoluble substances is Eq. (24). The activity of anions and cations can calculate the ionic product constant through Eq. (25). When the ion product constant is higher than the solution product constant, the scale form continuously. The results of the samples ion product constant and solution product constant are shown in Table 4. These water samples are likely to scale.

$$A_m B_n(s) \rightleftharpoons m A_{\mathrm{aq}}^{n+} + n B_{\mathrm{aq}}^{m-} \tag{24}$$

$$K_{\mathrm{sp}} = c_{A^{n+}}^m \times c_{B^{m-}}^n \tag{25}$$

where $c_{A^{n+}}$ is cationic molarity, $c_{A^{n+}}^m$ is the activity of cation, $c_{B^{m-}}$ is anionic molarity, $c_{B^{m-}}^n$ is the activity of anion, and K_{sp} is the solution product constant.

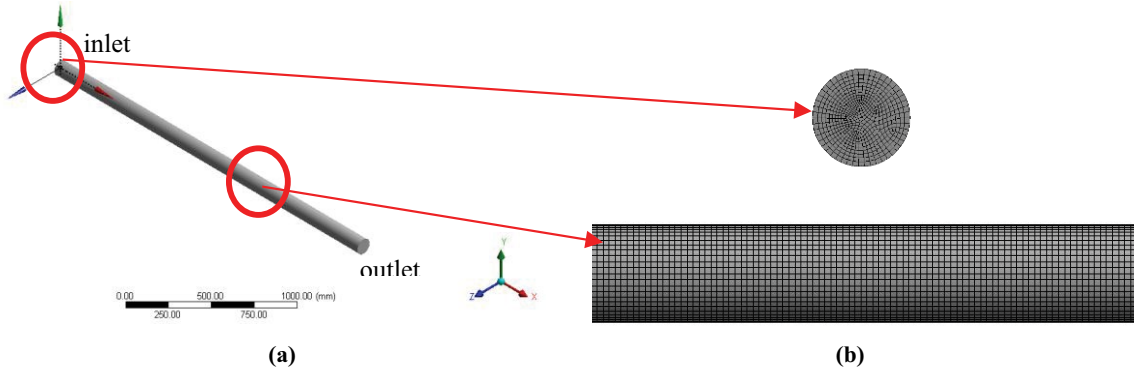

Fig. 4. Straight pipe schematics of (a) physical model and (b) mesh.

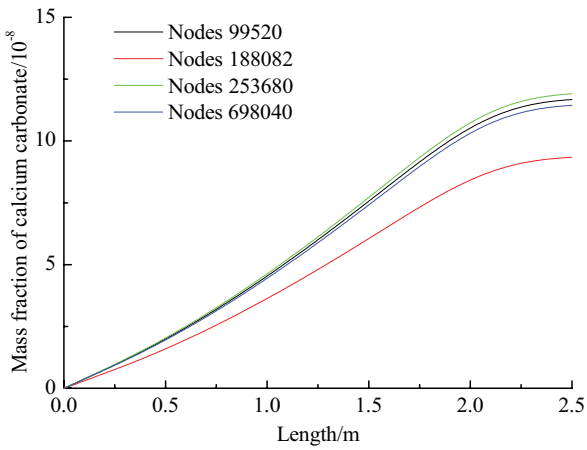

Fig. 5. Results of grid independence validation for straight pipe.

The mass of scaling at different temperatures are shown in Table 5, which revealed that the amount of scale increases with the increase of temperature. Due to the various components of produced water, the relationship between the amount of scale and temperature is varied. According to the mass of scaling at different temperatures, Eqs. (16)–18 can be used to obtain the A and β of the forward reaction rate [43], as shown in Table 6.

The microstructure of the station A scale surface is exhibited in Fig. 7a. The scale sample has a granular structure. From the results of the X-ray diffraction pattern, the high-temperature weightless method and EDS (Tables 7 and 8) show that the main composition is $CaCO_3$, which takes almost 86% in terms of the weight. The scale sample also contains about 6% corrosion scale. Based on the above analysis, the crystal type of scale samples is calcite, which is challenging to clear out due to the structure is relatively dense.

4.2. Numerical results

4.2.1. Straight pipe

Before examining the effect of factors, case 5 is selected as a standard case of straight pipe to make comparisons with other cases. The temperature distribution nephogram is exhibited in Fig. 8a. The temperature of the pipe wall is the lowest; the pipe axis is highest. The temperature gradient is more significant. Further analysis of the pipeline temperature data obtained by FLUENT software shows

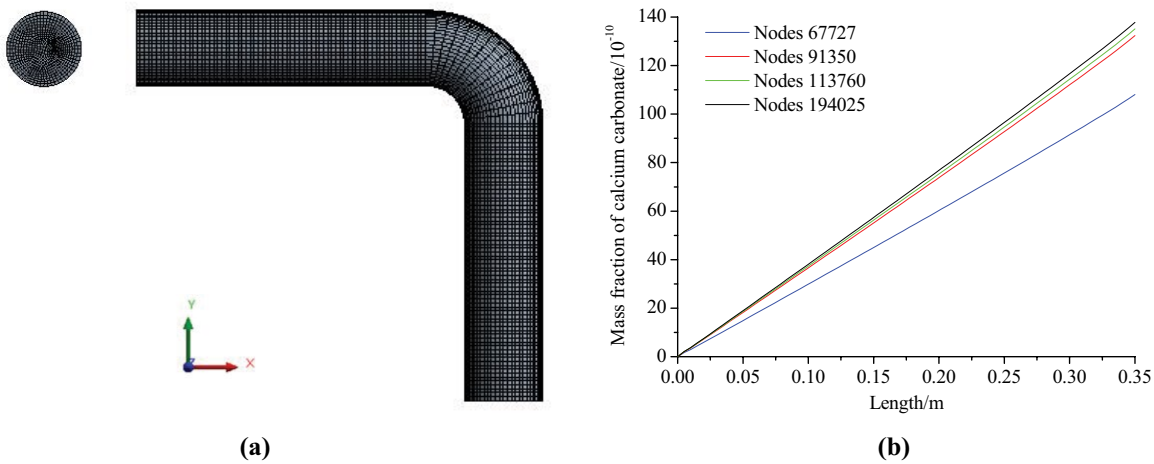

Fig. 6. Results of the elbow (a) grid division and (b) independent verification when the bending radius is 105 mm.

Table 1
Straight pipe simulation scheme

Case	Temperature (K)	Scale concentration (multiple)	Particle diameter (μm)	Inlet velocity (m s^{-1})
1	303.15	1	1	2.5
2	313.15	1	1	2.5
3	323.15	1	1	2.5
4	333.15	1	1	2.5
5	343.15	1	1	2.5
6	343.15	2	1	2.5
7	343.15	5	1	2.5
8	343.15	8	1	2.5
9	343.15	10	1	2.5
10	343.15	1	2	2.5
11	343.15	1	5	2.5
12	343.15	1	8	2.5
13	343.15	1	10	2.5
14	343.15	1	1	1.5
15	343.15	1	1	2.0
16	343.15	1	1	3.0
17	343.15	1	1	3.5

Table 2
Horizontal elbow section simulation scheme

Case	Temperature (K)	Bending radius (mm)	Inlet velocity (m s^{-1})
18	303.15	210	2.5
19	313.15	210	2.5
20	323.15	210	2.5
21	333.15	210	2.5
22	343.15	210	2.5
23	343.15	105	2.5
24	343.15	315	2.5
25	343.15	420	2.5
26	343.15	525	2.5
27	343.15	1	1.5
28	343.15	1	2.0
29	343.15	1	3.0
30	343.15	1	3.5

Table 3
Quality of produced water samples

Sample	1	2	3
pH	6.72	6.69	6.63
K^+/Na^+ (mg L^{-1})	27,800	29,100	24,600
Ca^{2+} (mg L^{-1})	1,760	1,660	2,040
Mg^{2+} (mg L^{-1})	186	215	260
Ba^{2+}/Sr^{2+} (mg L^{-1})	2,070	1,520	1,680
Cl^- (mg L^{-1})	47,700	48,900	49,100
SO_4^{2-} (mg L^{-1})	0.00	5.23	39.0
HCO_3^- (mg L^{-1})	527	517	361
Total salinity (mg L^{-1})	80,100	81,900	82,000
Water type	$CaCl_2$	$CaCl_2$	$CaCl_2$

that the temperature slightly decreases along the direction of the flow which is due to the heat transfer between the pipe wall and the external environment during the flow of the pipe, resulting in the loss of heat and the gradual decrease of temperature.

As shown in Fig. 8b, there is a significant difference in the flow between near the wall and away from the sidewall. The center of the pipeline has a maximum flow velocity. Particles move horizontally along the wall in the boundary layer due to the constraint of the wall. The viscous shear stress plays a leading role, and the velocity of fluid will decrease. At the same time, the closer to the wall, the velocity gradient is higher, indicating that the fluid velocity changes more violently in the adjacent wall area. According to the continuity equation, when the fluid speed at the wall boundary layer decreases, the corresponding other fluid velocities will be increased correspondingly. As a result of the fluid viscosity, the accelerated fluid will also drive the fluid in the boundary layer, causing the pressure gradient to appear in the wall.

The $CaCO_3$ distribution nephogram in the pipeline is shown in Fig. 9a. At the entrance of the pipe, $CaCO_3$ particles do not exist, but $CaCO_3$ particles e gradually generate in the process of the flow. With the flow of fluid, the mass fraction of $CaCO_3$ generated at 1.0 m reached a peak of 5.732×10^{-8}, with a deposition probability of 1.07%, and the actual deposition of $CaCO_3$ is 6.105×10^{-10}. The mass score of $CaCO_3$ generated by the former 1.0 m is 2.162×10^{-8},

Table 4
Results of the samples ion product constant and solution product constant

Sample	1	2	3
Ionization product of $CaCO_3$	3.863×10^{-5}	3.577×10^{-4}	3.068×10^{-4}
K_{sp} of $CaCO_3$	2.8×10^{-9}	2.8×10^{-9}	2.8×10^{-9}
Ionization product of $CaSO_4$	0	2.26×10^{-6}	2.07×10^{-5}
K_{sp} of $CaSO_4$	9.1×10^{-6}	9.1×10^{-6}	9.1×10^{-6}
Ionization product of $BaSO_4$	0	6.04×10^{-7}	4.98×10^{-6}
K_{sp} of $BaSO_4$	1.1×10^{-10}	1.1×10^{-10}	1.1×10^{-10}

Table 5
Mass of scaling at different temperatures (196 h)

Temperature (K)	303.15	313.15	323.15	333.15	343.15	353.15
Sample 1 (mg L^{-1})	2.312	4.303	5.264	6.041	6.750	7.442
Sample 2 (mg L^{-1})	0.007	2.481	3.842	4.279	5.708	6.393
Sample 3 (mg L^{-1})	0.009	2.509	3.960	4.723	5.797	7.812

Table 6
Reaction rate constant

Sample	1		2		3	
Ca^{2+} (mg L^{-1})	1,760		1,660		2,040	
HCO_3^- (mg L^{-1})	527		517		361	
Temperature (K)	343.15	333.15	343.15	333.15	343.15	333.15
Amount of scale (mg L^{-1})	6.750	6.041	5.708	4.279	5.797	4.723
10^{10} r (mol L^{-1} s^{-1})	0.9566	0.8562	0.8090	0.6060	0.8216	0.6694
10^4 C (L^2 mol^{-2} s^{-1})	3.209	2.872	2.714	2.034	4.600	3.747
A	1.319×10^{40}		7.194×10^{24}		1.673×10^{32}	
B	–12.826		–6.835		–9.650	

shown in Fig. 9b. $CaCO_3$ particles flow in the straight pipe by inertial force, drag force, gravity, buoyancy, Basset force, Magnus lift force, Saffman lift force, and the adsorption effect of the wall, $CaCO_3$ particle aggregation. But the larger the scouring action of fluid in a pipe, and will take away the $CaCO_3$ particles, leading to the content of $CaCO_3$ at the center of the pipe is far more than the wall in content.

4.2.2. Horizontal elbows

Before examining the effect of factors, case 22 is selected as a standard case of horizontal elbows to make comparisons with other cases. Fig. 10a indicates the velocity distribution nephogram. The velocity in the straight pipe section of the elbow reduces uniformly. However, the inner wall surface of the inlet of the elbow forms a high-speed area. The velocity of the lateral wall slightly decreases. When the fluid enters the elbow, due to the effect of centrifugal force, most of the fluid will be transferred to the outside of the elbow, resulting in lower lateral velocity and radial velocity gradient. A low-speed area forms near the inner wall of the exit when the fluid flows out of the elbow.

$CaCO_3$ particles are not present at the entrance of the straight pipe section, but a part of $CaCO_3$ particles generates along with the fluid flow, shown in Fig. 10b. Some $CaCO_3$ particles also deposit on the wall due to the adsorption effect of the wall. In the vicinity of the inner wall near the exit of the elbow (low-speed area), $CaCO_3$ high concentration area appears. Finally, the mass fraction of $CaCO_3$ is 2.957×10^{-8}. The scaling mass in the elbow of the same length is more than the straight pipe section. The chemical reaction rate and disposition probability will increase with the change of the track of scale-forming cation and scale-forming anion. The deposition probability reached 8.76%. The actual mass fraction of $CaCO_3$ deposition is 2.590×10^{-9}, which is more than the straight pipe.

4.3. Model validation and adaptability analysis

The experiment items measured the actual thickness of the scale layer and demonstrated the reliability of the CFD-SRCM [44]. A removable 40 cm long straight pipe and a horizontal elbow in which radius is 210 mm with the specification of DN100 was installed. The pipe segment operated for 218 d from October 31, 2015, to June 5,

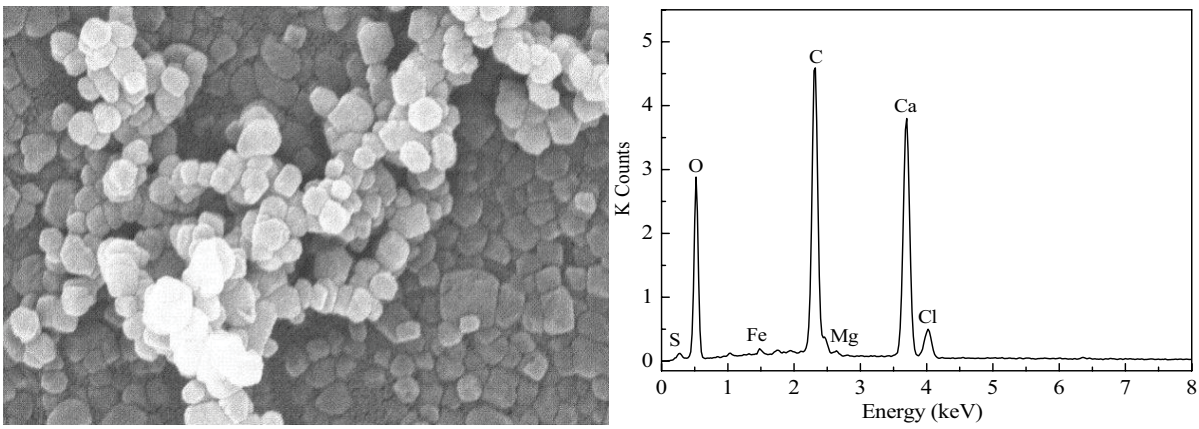

(a) (b)

Fig. 7. Station A scale (a) surface microstructure and (b) X-ray diffraction pattern.

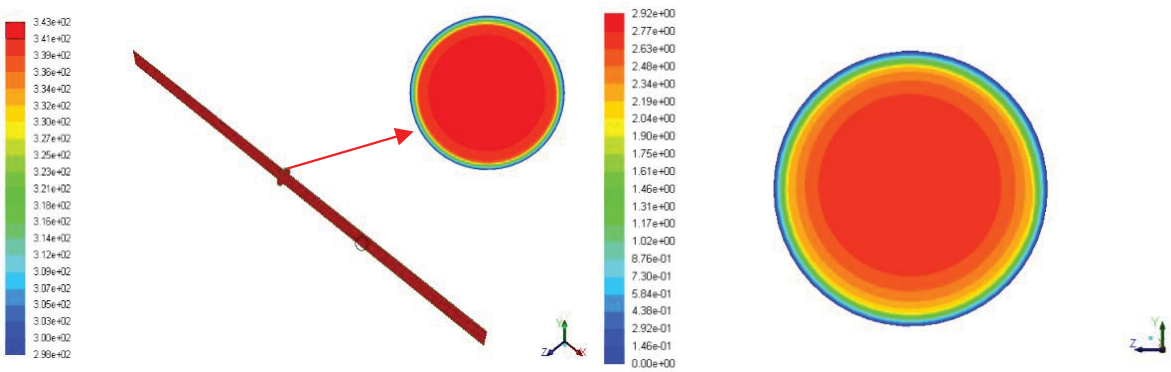

(a) (b)

Fig. 8. Distribution nephogram of (a) temperature (unit: K) and (b) velocity (unit: m s^{-1}).

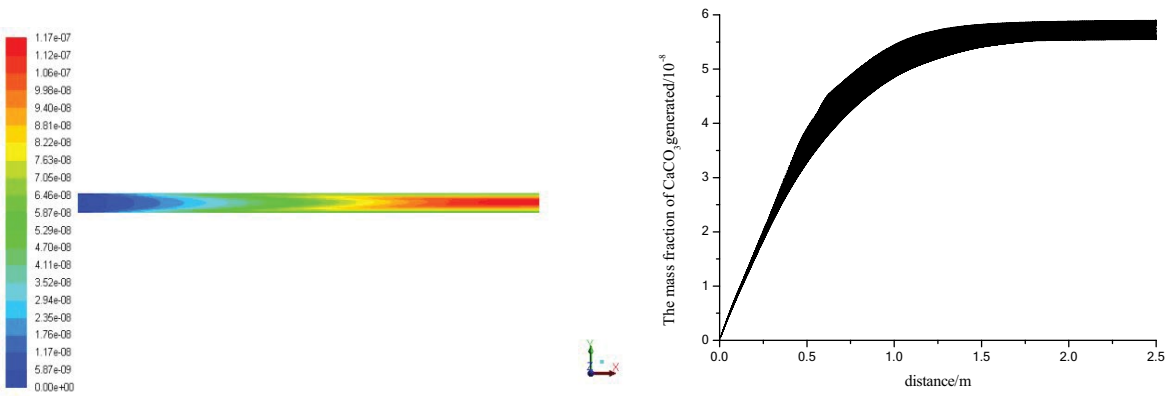

(a) (b)

Fig. 9. $CaCO_3$ mass fraction (a) distribution nephogram and (b) distribution along the *X*-axis.

2016. The metal pipe sections disassembled to observe the scaling phenomenon of the inner wall. There are apparent scaling phenomena in the inner wall of the pipeline, such as the lining of a uniform layer of silvery-white scale. The scale thickness of the straight pipe section is 1.5 to 1.8 mm. In particular, the scale thickness of the horizontal elbow can achieve 6.5 to 6.7 mm, shown in Fig. 11b. Calculated by Eqs. (19)–(22), the scale thickness of the straight pipe is 1.46 mm, and the scale thickness of the horizontal elbow is 6.20 mm when the bending radius is 210 mm, shown

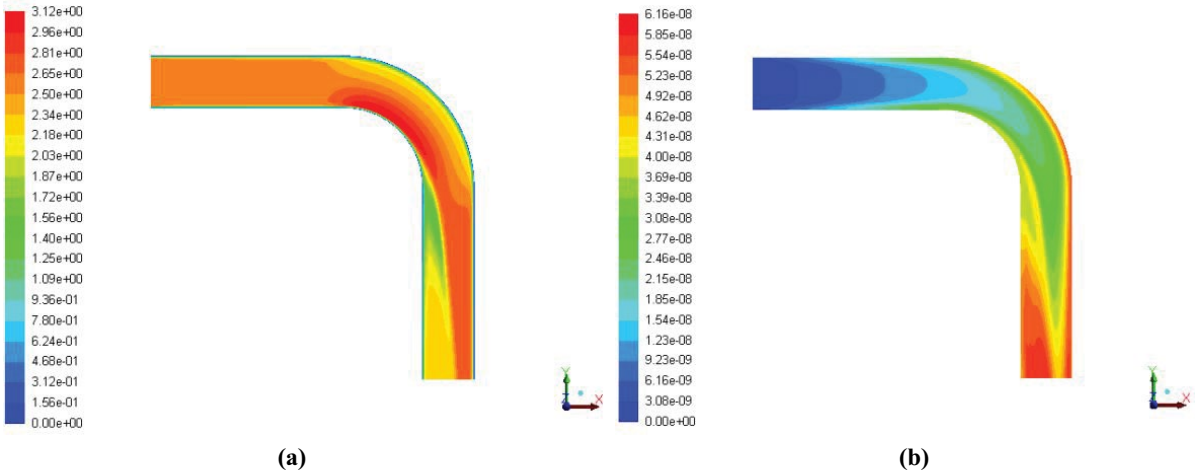

Fig. 10. Distribution nephogram of (a) velocity (unit: m s^{-1}) and (b) $CaCO_3$ mass fraction when the bending radius is 210 mm.

Table 7
Result of the high-temperature weightless method

Temperature (K)	Weight reduction (%)	Reduced substance
378.15	6.89	Free water
823.15	15.72	Organic matter, crystal water, bound water
1,223.15	29.34	Decomposition of inorganic matter such as carbonate and oxide

Table 8
Result of EDS

Element	wt. (%)	at. (%)
O	52.04	63.81
S	0.91	0.56
Ca	34.35	16.85
C	10.92	17.85
Fe	0.66	0.23
Mg	0.31	0.25
Cl	0.81	0.45

in Table 9. It leads to a decrease in the flow area to a certain extent. The comparison shows that the numerical simulation results are consistent with the actual situation. However, the numerical simulation only considers single-phase flow, and the flow velocity is unstable in actual pipeline operation, so there is a particular deviation in the calculation results. The relative difference between the real scale rate and the calculated value is in the range of 2.7% to 18.9%. Therefore, CFD-SRCM can accurately predict the scaling rate of $CaCO_3$ in wet-gas pipes.

The simulation of the external pipe of station A and station B can further analyze the adaptability of CFD-SRCM. The specifications of these two pipelines are DN150. The actual internal diameter is 146 mm, and the outer diameter is 168 mm. The lengths of the external pipe of the station A and station B are 6.11 and 7.88 km. The actual operating parameters and CFD-SRCM can calculate the scale rates of $CaCO_3$. The actual mass fraction of $CaCO_3$ deposition in the station A is 4.8327×10^{-8}, which station B is 4.3027×10^{-8}. Both deposition probabilities are 1.008%. Therefore, the exact deposition amount of $CaCO_3$ in the station A is 4.871×10^{-10}, and which in the station B is 4.337×10^{-10}. The scaling amount of the external pipe can be obtained by Eqs. (21) and (22), shown in Table 10.

Two industrial cases forecast the scaling rates. The station A pipeline is conducted on October 20, 2015, distance pigging operation last 160 d. The thickness of the scale layer is from 0.8 to 0.9 mm, and the model predicts that the scale thickness is 0.56 mm. The station B pipeline is conducted on August 24, 2015, distance pigging operation last 226 d. The ply of the scale layer is from 1.0 to 1.2 mm, and the model predicts that the scale thickness is 0.70 mm. The anticipated results are in good agreement with the actual situation. Therefore, CFD-SRCM is highly adaptable to other pipelines.

4.4. Effect of factors

4.4.1. Straight pipe

Under the temperature condition of the station A, the actual $CaCO_3$ deposition increases with the increase of temperature and growth quickly [22,35]. On the one hand, the solubility of $CaCO_3$ decreases with the rise in temperature, causing a large amount of $CaCO_3$ suspended particles in the fluid. On the other hand, the chemical reaction (Eq. (2)) is the exothermic reaction. The chemical reaction equilibrium will move in the direction of the generate $CaCO_3$ with the increase of temperature, further promoting

Table 9
Scaling of each local component

Local components	Temperature (K)	Inlet velocity (m s^{-1})	Scale amount (mg h^{-1})	Scale thickness (mm)
Straight pipe	343.15	2.5	2.259	1.46
Horizontal elbow (210 mm)	343.15	2.5	9.585	6.20

Table 10
Scaling amount of the external pipe

Station	Temperature (K)	Inlet velocity (m s^{-1})	Scale amount (mg h^{-1})	Scale thickness (mm)	Daily scale amount (kg)
A	303.15	1.5	0.9014	1.74×10^{-3}	0.0881
B	303.15	1.5	0.8025	1.55×10^{-3}	0.1012

Fig. 11. Scaling phenomena of (a) the horizontal elbow, (b) the straight pipe, and the external pipeline of (c) the station A, and (d) the station B.

the deposition of $CaCO_3$ particles. Therefore, the temperature has a significant influence on the scaling rate.

Fig. 12b presents the concentration of scale ions is changed to n times; the actual deposition of $CaCO_3$ is about n times. Further, the curve is fitted by ORIGIN software to obtain the equation of the curve:

$$\omega_{ws} = 6.14066c_{si} - 0.06245 \tag{26}$$

where ω_{ws} is the $CaCO_3$ mass score of deposition, c_{si} is the concentration of scale ions.

The concentration of scale ions is roughly linear function relation with the generated $CaCO_3$ mass fraction, but the

slope is more than 6.105. As the concentration of scale ions increases, the chemical reaction will move to the right to promote the formation of scale.

Fig. 12c displays the particle diameter in the DPM model is independent of the $CaCO_3$ mass fraction of the precipitation because of the $CaCO_3$ particles in the model generated by a chemical reaction rather than injected by the DPM model through the entrance.

The deposition of $CaCO_3$ decreases with the increase of inlet velocity and the downward trend reduces, shown in Fig. 12d. The larger the inlet velocity, the higher the carrying capacity of the fluid in the pipeline to $CaCO_3$ particles, and the more likely to wash the deposited $CaCO_3$ particles.

4.4.2. Horizontal elbows

The relationship between the deposition quantity in the horizontal elbow and the straight pipeline can analyzes from the perspective of hydrodynamics by CFD-SRCM. The influence rule is similar to the straight pipe. But the scaling rate of $CaCO_3$ in the horizontal elbow is higher than the straight pipe due to the collide probability of scale ions increases when the fluid moves to the elbow. The chemical reaction is natural to occur, and $CaCO_3$ particles generate.

Fig. 13 displays the velocity gradient, and the range of low-speed area decreases with the growth of the bending radius. With the increase of bending radius, the mass fraction and the deposition probability of $CaCO_3$ in the pipeline gradually increases due to $CaCO_3$ particles have a smaller velocity gradient when they are moving in the bigger bending of the elbow, as shown in Fig. 14. The erosion effect of the fluid on the lateral deposition of $CaCO_3$ particles decreased, which increased the deposition probability of $CaCO_3$ particles on the wall. The migration time of $CaCO_3$ particles in the elbow increases and the actual deposition amount will increase correspondingly.

5. Conclusion

The scaling rate rules of produced water are mainly from the perspective of thermodynamics, without considering the hydrodynamic factors. Therefore, CFD-SRCM considering both thermodynamic and hydrodynamic is established to predict the scaling rate of the wet-gas pipes based on experimental research, theoretical analysis, and numerical simulation. Main understandings are as follows:

- Experiments show that the water samples contained higher concentrations of scale ions; these included Ca^{2+},

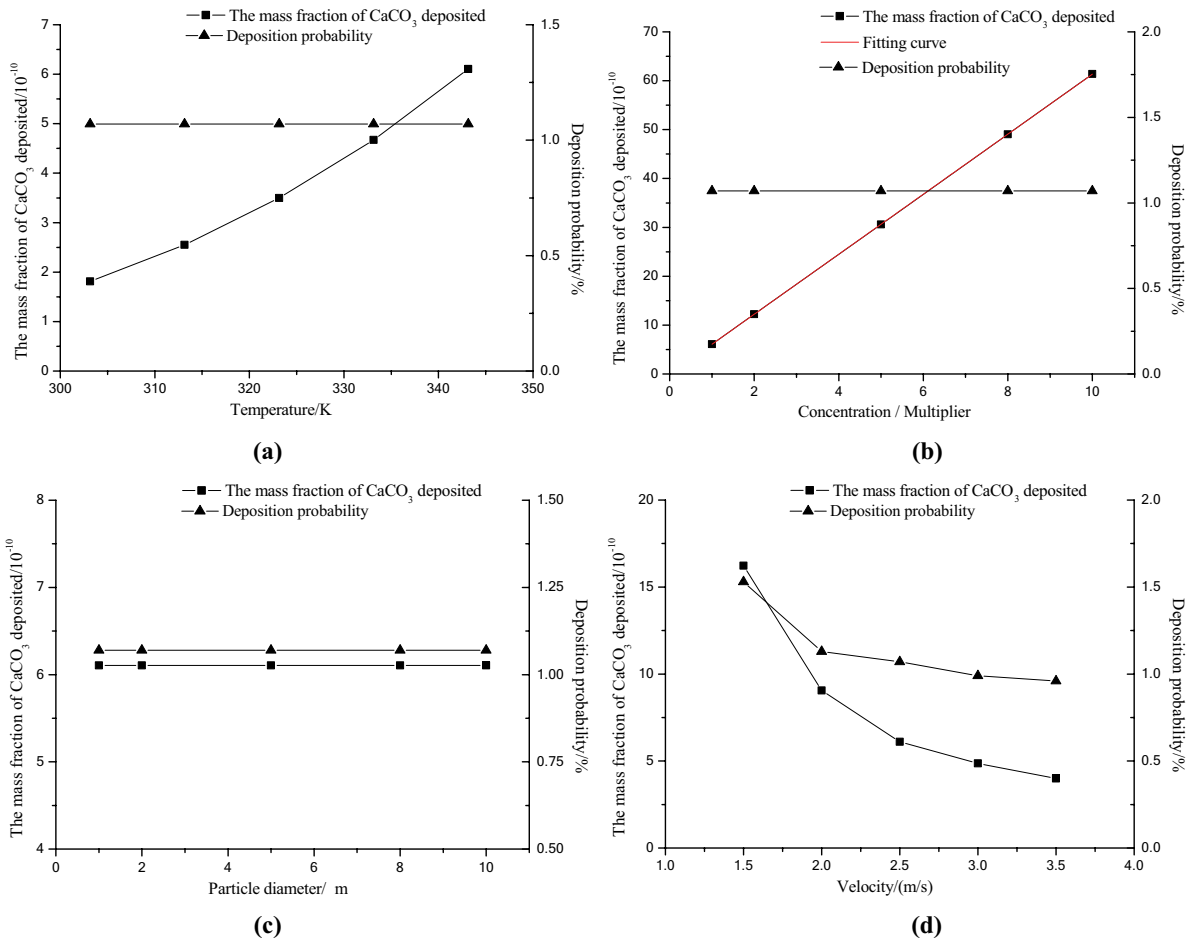

Fig. 12. Influence rule curve of (a) temperature, (b) scale ion concentration, (c) particle size, and (d) inlet velocity on deposition quantity and deposition probability of $CaCO_3$.

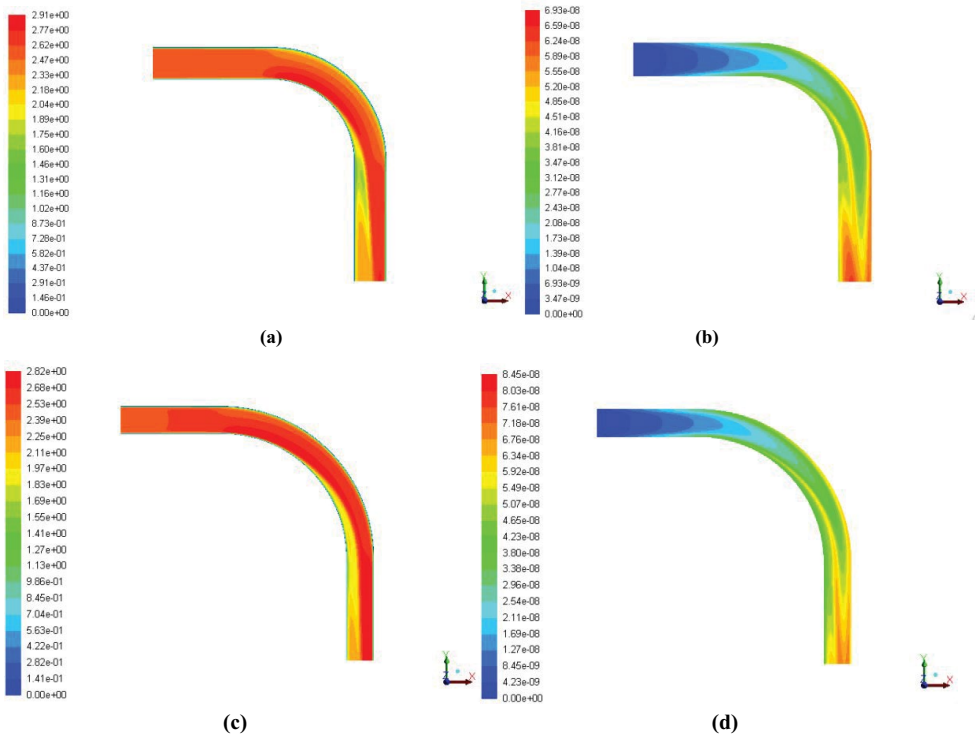

Fig. 13. Distribution nephogram of velocity (m s^{-1}) and $CaCO_3$ mass fraction when the bending radii are 315 mm (a and b) and 525 mm (c and d).

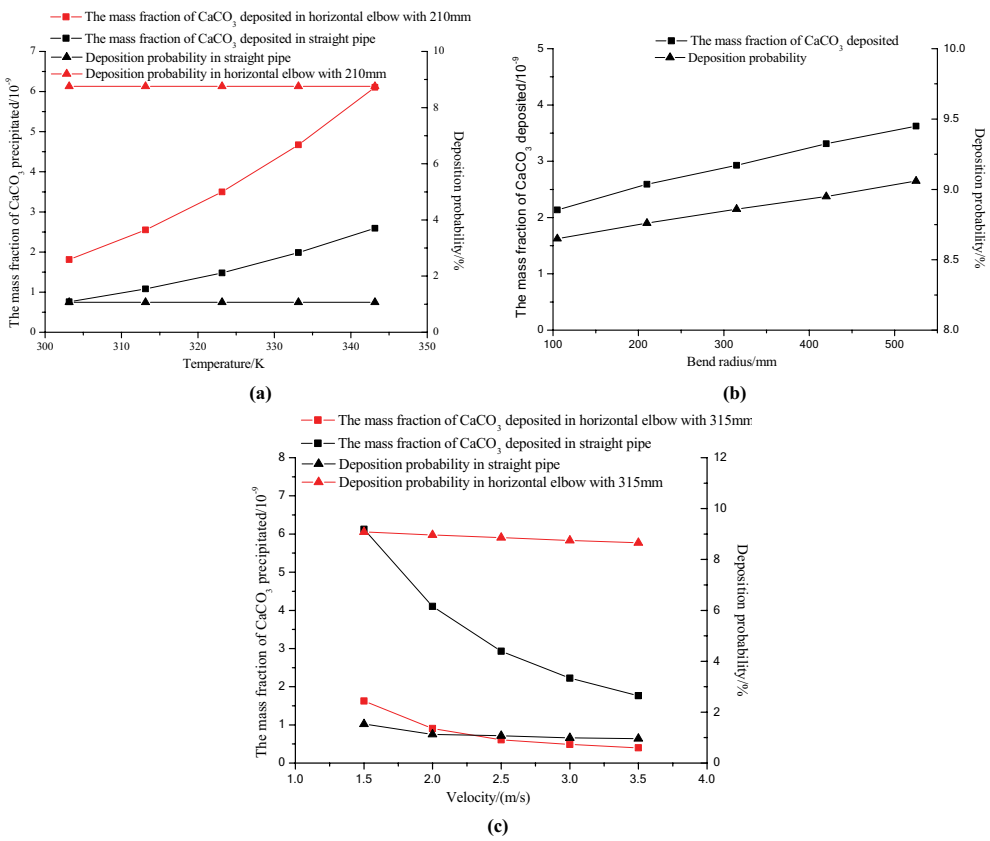

Fig. 14. Influence rule curve of (a) temperature, (b) bending radius, and (c) inlet velocity on deposition quantity and deposition probability of $CaCO_3$.

Mg^{2+}, Ba^{2+}, Sr^{2+} cations, and HCO_3^-, SO_4^{2-} anions. The main composition of the scale is $CaCO_3$, containing a small amount of corrosion. The two key parameters, A and β, fit from the mass of scaling at different temperatures.

- Scale deposition mechanism of the $CaCO_3$ scale in the wet-gas pipe is the formation of $CaCO_3$ particles through the chemical reaction, crystallization, precipitation, and deposition.
- CFD-SRCM can simulate the scale formation and deposition process, and quickly and accurately predict the scaling rate in straight pipes and horizontal elbows. The experiment items study for wet-gas pipelines demonstrates CFD-SRCM. The relative deviation between the actual scale rate and the calculated value is in the range of 2.7% to 18.9%. Two industrial cases attest that CFD-SRCM owns highly adaptable to other pipelines.
- Scaling rate of $CaCO_3$ increases with the growth of temperature, scale ion concentration, and bending radius while the inlet velocity is the opposite. And it is independent of the setting $CaCO_3$ particle diameter. The effects of the straight pipe and the horizontal elbows parameters further demonstrates CFD-SRCM.

The model represents a highly promising new way method for predictive monitoring of scaling. CFD-SRCM can quickly and accurately predict the scaling rate of $CaCO_3$ in wet-gas pipes. This allows early detection of acute deposition periods and early diagnosis of the likely causes and supports remedial decision making.

Symbols

A	—	Exponential factor
A_{face}	—	Projected area of scale particles on the wall
$c_{Ca^{2+}}$	—	Ca^{2+} ion concentration, mol L^{-1}
$c_{HCO_3^-}$	—	HCO_3^- ion concentration, mol L^{-1}
C	—	Reaction rate constant, L^2 mol^{-2} s^{-1}
C_D	—	Drag coefficient
C_f	—	Forward reaction rate constant
C_p	—	Specific heat capacity, J kg^{-1} K^{-1}
c_{si}	—	Concentration of scale ions
d_{in}	—	Diameter of pipe inlet surface, m
d_p	—	Diameter of particle
E	—	Activation energy, 46,600 J mol^{-1}
g	—	Gravitational acceleration, m s^{-2}
G_k	—	Turbulent kinetic energy caused by the mean velocity gradient
k	—	Conduction coefficient
l	—	Thickness of the scale layer, mm
m	—	Mass
m_{ds}	—	daily scale amount of $CaCO_3$, mg h^{-1}
m_f	—	Actual deposition of $CaCO_3$ mass fraction
m_p	—	Resulting $CaCO_3$ mass fraction
m_{pv}	—	$CaCO_3$ particle mass flow velocity, kg s^{-1}
M_{CaCO_3}	—	Molecular mass of $CaCO_3$, 100 g mol^{-1}
M_p	—	Particle mass
N	—	Number of particles
p	—	Pressure
r	—	Reaction rate, mol L^{-1} s^{-1}
R	—	Gas constant, 8.314 J mol^{-1} K^{-1}
Re	—	Reynolds number
S_M	—	Source term of the mass equation
S_{MO}	—	Source term of momentum equation
S_E	—	Source term of the energy equation
t	—	Time, d
T	—	Temperature, K
u	—	Velocity, m s^{-1}
v_d	—	Deposition rate
v_r	—	Denudation rate
x	—	Length

Greek

α	—	Impact angle of particles on the wall surface
β	—	Temperature index
γ	—	Prandtl number
ρ_L	—	Density of fluid, 1.028 g cm^{-3}
ρ_p	—	Scale particles density, 2.71 g cm^{-3}
η	—	$CaCO_3$ particle volume concentration
ε	—	Energy dissipation rate
Δt	—	Time interval, s
μ	—	Hydrodynamic viscosity, Pa s
ϕ_{dep}	—	Probability of particles deposition
ω_{ws}	—	$CaCO_3$ mass score of deposition

Subscripts

eff	—	Effective
E	—	Energy
i	—	Average component in i direction
ip	—	Pulsation component in i direction
in	—	Inlet
j	—	Average component in j direction
jp	—	Pulsation component in j direction
k	—	Equation k
M	—	Mass
MO	—	Momentum
p	—	Particle
run	—	Pipeline running
trap	—	Captured (deposited) by the wall of the pipeline
escape	—	Escaped from the exit

References

[1] L. Clay, J. Pichtel, Treatment of simulated oil and gas produced water via pilot-scale rhizofiltration and constructed wetlands, Int. J. Environ. Res., 13 (2019) 185–198.

[2] S.J. Maguire-Boyle; A.R. Barron, Organic compounds in produced waters from shale gas wells, Environ. Sci. Processes Impacts, 16 (2014) 2237–2248.

[3] J.L. Li, T.D. Li, J.D. Yan, X.W. Zuo, Y. Zheng, F. Yang, Silicon Containing Scale Forming Characteristics and How Scaling Impacts Sucker Rod Pump in ASP Flooding, Proceeding of the Asia Pacific Oil and Gas Conference and Exhibition, Society of Petroleum Engineers, Jakarta, Indonesia, 2009, pp. 3–5.

[4] A.R. Al Salami, A.A.M.A. Kader, Downhole and Topside Scale Challenge-Removal, Prevention and Inhibition Strategy, Abu Dhabi International Petroleum Exhibition and Conference, Society of Petroleum Engineers, Abu Dhabi, UAE, 2010, pp. 1334–1351.

[5] W. Dickinson, L. Sanders, J. Kemira, Novel Barium Sulfate Scale Inhibitor for Use in High Iron Environments, Proceedings of the SPE Latin America and Caribbean Petroleum Engineering Conference, Society of Petroleum Engineers, Mexico City, Mexico, 2012, pp. 1588–1592.

[6] P. Zhang, Z. Zhang, Y. Liu, A.T. Kan, M.B. Tomson, Investigation of the impact of ferrous species on the performance of common oilfield scale inhibitors for mineral scale control, J. Petrol. Sci. Eng., 172 (2019) 288–296.
[7] D.Q. Kern, R.E. Seaton, A theoretical analysis of thermal surface fouling, Br. Chem. Eng., 4 (1959) 258–262.
[8] D.Q. Kern, R.E. Seaton, Surface fouling: how to limit, Chem. Chem. Eng. Prog., 55 (1959) 71–73.
[9] D. Hasson, Rate of decrease of heat transfer due to scale deposition, Dechema-Monographien, 47 (1962) 233–282.
[10] D. Hasson, M. Avriel, W. Resnick, T. Rozenman, S. Windreich, Mechanism of calcium carbonate scale deposition on heat-transfer surfaces, Ind. Eng. Chem. Fundam., 7 (1968) 59–65.
[11] M. Amiri, J. Moghadasi, M. Jamialahmadi, M.P. Shahri, Prediction of the amount of calcium carbonate scale formation in Iranian oilfields at different pressures, Energy Sources Part A, 35 (2013) 1197–1209.
[12] A. Kamari, F. Gharagheizi, A. Bahadori, A.H. Mohammadi, Determination of the equilibrated calcium carbonate (calcite) scaling in aqueous phase using a reliable approach, J. Taiwan Inst. Chem. Eng., 45 (2014) 1307–1313.
[13] G.V. Chilingar, R. Mourhatch, G.D. Al-Qahtani, The Fundamentals of Corrosion and Scaling for Petroleum & Environmental Engineers, Gulf Publishing Company, Houston, TX, 2008.
[14] A.E. Nielsen, The kinetics of crystal growth in barium sulfate precipitation. II. Temperature dependence and mechanism, Acta Chem. Scand., 13 (1959) 784–802.
[15] P.G. Bedrikovetsky, R.P. Lopes, F.F. Rosario, M.C. Bezerra, E.A. Lima, Oilfield Scaling - Part I: Mathematical and Laboratory Modelling, Proceedings of the SPE Latin American and Caribbean Petroleum Engineering Conference, Society of Petroleum Engineers, Port-of-Spain, Trinidad and Tobago, West Indies, 2003, pp. 1–13.
[16] P.G. Bedrikovetsky, R.P. Lopes, P.M. Gladstone, F.F. Rosario, M.C. Bezerra, E.A. Lima, Barium Sulphate Oilfield Scaling: Mathematical and Laboratory Modelling, Proceedings of the SPE International Symposium on Oilfield Scale, Society of Petroleum Engineers, Aberdeen, UK, 2004, pp. 1–13.
[17] O.J. Vetter, V. Kandarpa, A. Harouaka, Prediction of scale problems due to injection of incompatible waters, J. Petrol. Technol., 34 (1982) 273–284.
[18] A.T. Kan, M.B. Tomson, Scale prediction for oil and gas production, SPE J., 17 (2012) 362–378.
[19] F. Brahim, W.G. Augustin, M. Bohnet, Numerical simulation of the fouling process, Int. J. Therm. Sci., 42 (2003) 323–334.
[20] S.G. Johnsen, S.T. Johansen, B. Wittgens, A Wall-Function Approach for Direct Precipitation/Crystallization Fouling in CFD Modelling, Proceedings of International Conference on Heat Exchanger Fouling and Cleaning, Enfield (Dublin), Ireland, 2015, pp. 198–206.
[21] J. Xiao, Z.H. Li, J. Han, F. Pan, M.W. Woo, X.D. Chen, A systematic investigation of the fouling induction phenomena with artificial crystal structures and distributions, Chem. Eng. Sci., 168 (2017) 137–155.
[22] S.T.W. Kuruneru, E. Sauret, S.C. Saha, Y.T. Gu, Coupled CFD-DEM simulation of oscillatory particle-laden fluid flow through a porous metal foam heat exchanger: mitigation of particulate fouling, Chem. Eng. Sci., 179 (2018) 32–52.
[23] A.R.C. Souza, A.L.H. Costa, Modeling and simulation of cooling water systems subjected to fouling, Chem. Eng. Res. Des., 141 (2019) 15–31.
[24] M. El-Said, M. Ramzi, T. Abdel-Moghny, Analysis of oilfield waters by ion chromatography to determine the composition of scale deposition, Desalination, 249 (2009) 748–756.
[25] A. Khormali, D.G. Petrakov, M.J.A. Moein, Experimental analysis of calcium carbonate scale formation and inhibition in waterflooding of carbonate reservoirs, J. Petrol. Sci. Eng., 147 (2016) 843–850.
[26] W. Tang, Y.H. Lin, S.Y. Ma, K. Huang, T.J. Yao, F. Li, S.S. Chen, The scaling mechanism of glass fiber reinforced plastics pipeline, J. Petrol. Sci. Eng., 159 (2017) 522–531.
[27] T. Yi, Z. Jin, X. Chuan-Li, W. Wei-Ying, A Bohai sea SZ36-1 oil field formation scaling experimental study and scale inhibitor optimization, Petrol. Sci. Technol., 32 (2014) 2512–2519.
[28] W. Keogh, A. Neville, M. Huggan, V. Eroini, J.H. Olsen, F.M. Nielsen, S. Baraka-Lokmane, E. Bourdelet, J.A. Ellingsen, O. Bache, T. Charpentier, Deposition of inorganic carbonate, sulfate, and sulfide scales on antifouling surfaces in multiphase flow, Energy Fuels, 31 (2017) 11838–11851.
[29] M.S. Khan, M.O. Budair, S.M. Zubair, A parametric study of $CaCO_3$ scaling in AISI 316 stainless steel tubes, Heat Mass Transfer, 38 (2001) 115–121.
[30] A.B. BinMerdhah, A.A. Mohd Yassin, M.A. Muherei, Laboratory and prediction of barium sulfate scaling at high-barium formation water, J. Petrol. Sci. Eng., 70 (2010) 79–88.
[31] B. Senthilmurugan, B. Ghosh, S. Sanker, High performance maleic acid based oil well scale inhibitors—development and comparative evaluation, J. Ind. Eng. Chem., 17 (2011) 415–420.
[32] A.A. Olajire, A review of oilfield scale management technology for oil and gas production, J. Petrol. Sci. Eng., 135 (2015) 723–737.
[33] A. Neville, Surface scaling in the oil and gas sector: understanding the process and means of management, Energy Fuels, 26 (2012) 4158–4166.
[34] D. Buhmann, W. Dreybrodt, The kinetics of calcite dissolution and precipitation in geologically relevant situations of karst areas: 1. Open system, Chem. Geol., 48 (1985) 189–211.
[35] C.W. Lei, Z.X. Peng, T. Day, X.P. Yan, X.Q. Bai, C.Q. Yuan, Experimental observation of surface morphology effect on crystallization fouling in plate heat exchangers, Int. Commun. Heat Mass Transfer, 38 (2011) 25–30.
[36] S. Muryanto, A.P. Bayuseno, H. Ma'mun, M. Usamah, Jotho, Calcium carbonate scale formation in pipes: effect of flow rates, temperature, and malic acid as additives on the mass and morphology of the scale, Procedia Chem., 9 (2014) 69–76.
[37] M. Reiche, S. Grahl, M. Beckmann, Advanced monitoring of the fouling process on water walls, Fuel, 216 (2018) 436–444.
[38] S.-Z. Tang, F.-L. Wang, Q.L. Ren, Y.-L. He, Fouling characteristics analysis and morphology prediction of heat exchangers with a particulate fouling model considering deposition and removal mechanisms, Fuel, 203 (2017) 725–738.
[39] H.J. Zhu, Y.B. Tang, J. Wang, L.S. Tang, Flow erosion and flow induced vibration of gas well relief line with periodic fluctuation of boosting output, J. Loss Prev. Process Ind., 46 (2017) 69–83.
[40] N. Farnoosh, K. Adamiak, G.S.P. Castle, 3-D numerical analysis of EHD turbulent flow and mono-disperse charged particle transport and collection in a wire-plate ESP, J. Electrostat., 68 (2010) 513–522.
[41] I. Kimura, T. Hosoda, A non-linear k-ε model with realizability for prediction of flows around bluff bodies, Int. J. Numer. Methods Fluids, 42 (2003) 813–837.
[42] G.C. Pereira, F.J. de Souza, D.A. de Moro Martins, Numerical prediction of the erosion due to particles in elbows, Powder Technol., 261 (2014) 105–117.
[43] Z.H. Quan, Y.C. Chen, C.F. Ma, Experimental study of fouling on heat transfer surface during forced convective heat transfer, Chin. J. Chem. Eng., 16 (2008) 535–540.
[44] E. Diaz-Bejarano, E. Behranvand, F. Coletti, M.R. Mozdianfard, S. Macchietto, Organic and inorganic fouling in heat exchangers: industrial case study analysis of fouling rate, Ind. Eng. Chem. Res., 58 (2019) 228–246.